TOC

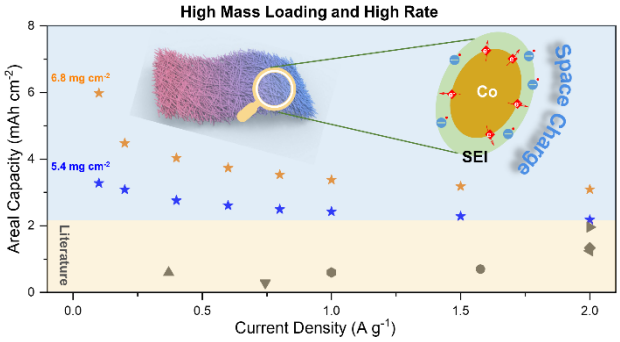

Inducing spin charge with zero stress ensures the creation of a high rate and areal capability for lithium storage.

Spin charge of Co nanoparticles loaded on the carbon substrate enabling rate-capable lithium storage at high mass-loadings

Bin Wang,[a] Xiaoling Teng,[a] Xiangkun Li,[b] Wanli Wang,[a] Hengjun Liu,[b] Zhiqiang Zhao,[b] Yuqi Li,[a] Deyu Kong,[a] Yi Wan,[a] Qiang Li,[b] Alistair J. Fielding,[c] Nuria Tapia Ruiz,[d] Han Hu, [a] and Mingbo Wu[a]*

[a] State Key Laboratory of Heavy Oil Processing, College of Chemistry and Chemical Engineering, China University of Petroleum (East China), Qingdao 266580, P. R. China

[b] College of Physics, University-Industry Joint Center for Ocean Observation and Broadband Communication, Qingdao University, Qingdao 266071, P. R. China

[c] Centre for Natural Products Discovery, School of Pharmacy and Biomolecular Sciences, Liverpool John Moore University, Byrom Street, Liverpool, L3 3AF, UK

[d] Department of Chemistry, Molecular Sciences Research Hub, White City Campus, Imperial College London, London, W12 0BZ, UK

Corresponding Authors:

hhu@upc.edu.cn (H. Hu),

Abstract

Developing high mass-loading electrodes is crucial for enhancing the energy density of current batteries, yet challenges such as poor rate performance and cycling instability must be addressed. Spin charge storage on transition metal nanoparticle surfaces, characterized by rapid charging and no phase transitions, offers an ideal storage behaviour for high mass-loading electrodes. In this study, we utilize electrospinning to fabricate free-standing carbon nanofibers incorporating Co nanoparticles for high mass loading and high-performance anodes. The resulting anode, with a maximum mass loading of 6.8 mg cm^{-2}, exhibits remarkable cycle stability and high-rate performance of 2 A g^{-1} at a capacity over 3 mAh cm^{-2}， superior than reported results. Magnetometry and electron paramagnetic resonance spectroscopy are employed to monitor the charge storage mechanism of the Co@CNFs, involving both the reversible formation of a spin capacitor and the growth of radical anions in the solid electrolyte interface at low voltages. Additionally, in situ X-Ray Diffraction and optical microscopy provide direct evidence of the absence of mechanical stress-induced phenomena within the spin charge process, attributed to high-rate capable lithium storage under high mass loading. The strategic approach presented herein offers a reliable methodology for engineering high-energy-density lithium-ion batteries.

Introduction

Lithium-ion batteries, possessing the remarkable high energy density, represent a pivotal class of energy storage devices crucial for advancing the large-scale utilization of clean electrical energy.[1, 2] While graphite is predominantly employed as the anode material in lithium-ion batteries, enabling reversible lithium ion storage, its intrinsic limitations in capacity, closely approaching the theoretical maximum (372 mAh g^{-1}), impose restrictions on the potential performance enhancements for graphite-based systems.[3, 4] In contrast, electrode materials employing alloying or conversion mechanisms offer higher capacity; however, the severe volume changes during lithium ion insertion/extraction compromise their stability and pose challenges in achieving prolonged cycle life.[5, 6] As a consequence, the simultaneous attainment of high mass loading, high capacity, high rate capability, and high stability in lithium anodes continues to be an immensely challenging endeavour.[7]

Recently, a groundbreaking advancement by Li et al. has introduced a cutting-edge in-situ magnetism characterization technique to investigate the lithium storage behaviour of iron, cobalt, and nickel oxides.[8] Remarkably, the outcomes of their research unveiled the presence of ultrafine metal nanoparticles formed in situ at the solid electrolyte interphase (SEI) interface, boasting an abundance of lithium ion storage sites. Under the influence of low potential, these metal nanoparticles harbour a significant number of vacant 3d orbitals for spin capacitance, enabling the accommodation of additional electrons, thereby establishing a spatial charge storage region within the SEI film.[8-11] Intriguingly, these findings not only corroborate the theoretical predictions of Maier et al.[12] but also signify a remarkable discovery in the field. Furthermore, these metal nanoparticles display an ability to transfer electrons to the SEI film, instigating the formation of negatively charged organic components, akin to the attributes of organic electrode materials.[13-15] By engaging in interface lithium storage, wherein the electrode material remains unaffected by volumetric and structural changes, this mechanism demonstrates distinct capacitive traits, thereby boasting unparalleled rate performance and exhibiting immense promise for the development of anode materials that simultaneously embody high capacity, high rate capability, and high stability.

Despite the identification of efficient lithium storage sites at the transition metal/SEI film, the fabrication of electrodes rich in metal nanoparticles and SEI film still presents challenges related to nanoparticle agglomeration and non-uniform

dispersion on the current collector. Additionally, the controllability of synthesizing ultrafine transition metal nanoparticles and achieving desirable SEI film properties remains an area of concern. Conventional electrode coating processes involving copper foil as the current collector often lead to weak interactions between the current collector and the active material,[16, 17] resulting in non-uniform aggregation of the active material and inadequate lithium storage interfaces between metal nanoparticles and the SEI film, consequently yielding a low anode loading.[16-19] In contrast, the implementation of three-dimensional carbon fibres fabricated through electrospinning offers distinct advantages, such as a high specific surface area, enabling the construction of electrodes with elevated active material loading.[20, 21] Recently, our group harnessed this technique to produce high-loading Fe site-modified carbon nanofibers (8 mg cm^{-2}), showcasing an area capacity of 1.76 mAh cm^{-2} at 7.1 mA cm^{-2}.[22] Furthermore, the interconnected porous structure of these fine carbon fibres plays a pivotal role in the creation of numerous metal/SEI film interfaces, consequently facilitating a high lithium storage capacity in the negative electrode material. Notably, recent findings by Hu et al. demonstrated that intrinsic defects on the surface of carbon materials effectively stabilize ultrafine metal nanoparticles, thereby preventing particle agglomeration during electrochemical applications[23], which ultimately contributes to enhanced electrode performance[24].

In this study, a simple electrospinning-thermal conversion strategy was employed to introduce metal Co nanoparticles into carbon fiber membranes to achieve high mass loading anodes for lithium storage. The interconnected mesh-like structure among the nanofibers served as efficient pathways for rapid electron and ion transport, thus exhibits an impressive areal capacity of 5.98 mAh cm^{-2} with the mass loading reach to 6.8 mg cm^{-2}, and 3 mAh cm^{-2} even under 2 A g^{-1}. Additionally, the distinctive spin-charge process of metal Co contributed to maintaining the structural integrity of the electrode and enhancing its cycling stability. In situ X-Ray Diffraction (XRD) and magnetometry measurements combined with the ex situ electron paramagnetic resonance (EPR) spectroscopy were conducted to understand the spin charge mechanism. Furthermore, the structural evolution of the high mass loading Co@CNFs electrodes during cycling was thoroughly investigated via the in situ optical microscopy.

Results and Discussion

Co@CNFs electrode were synthesized through a straightforward electrospinning-

thermal conversion process, where metal Co nanoparticles were introduced into polyacrylonitrile (PAN) nanofiber membranes (Figure S1). By carefully tuning the dosage of the spinning solution, high mass loading Co@CNFs (Co-modified carbon nanofibers) electrodes with varying thicknesses were successfully fabricated. Different from the smooth surface of CNFs (Seen Characterization 2.1 in SI, Figure S2), the Co@CNFs nanofiber exhibits a rougher texture (Seen Characterization 2.2 in SI, Figure S7 a and b) with the uniform distribution of metal Co particles (High-angle annular dark-field transmission electron microscopy (TEM) in Figure S8) ranging from 10 to 60 nm (Figure 1a) with a spacing of approximately 0.204 nm of the (111) crystal plane of metallic Co (Figure 1b). Thus, the Co@CNFs membrane electrode is woven from interlaced nanofiber (Figure S7 c and d), ensuring an increased specific surface area of 100.2 m^2 g^{-1} with rich mesopores (Figure S11) comparing with the pure CNFs (5.2 m^2 g^{-1}, Figure S5). This unique structure features an abundance of pores that facilitate efficient electrolyte infiltration and offer a rich array of electrochemical reaction sites. Additionally, the electrospinning technique ensures uniform thickness of the fibre membrane, enabling precise control over the electrode's quality.

The carbon material in both materials shows an amorphous structure (Figure S3 and Figure S4a for CNFs, Figure S9a for Co@CNFs)[25], and is enriched with oxygen functional groups containing C-OH, C=O, and COOH (Figure S10 c and d)[26, 27]. The I_D (disordered or defective structures, 1368 cm^{-1} in Raman spectra in Figure S6) /I_G (ordered graphite structures, 1599 cm^{-1} in Raman spectra in Figure S6)[28-30] ratio for Co@CNFs (1.12) is higher than that of CNFs (0.92), signifying a reduction in long-range order and an increase in structural defects within Co@CNFs. These defects play a crucial role in stabilizing the formation of ultrafine metal nanoparticles.[23, 24] The CNFs shows a single Lorentzian electron paramagnetic resonance (EPR) signal with the linewidth of 16.5 G (Figure S4b). The g value of CNFs is 2.0041, slightly higher than free electron (2.0023), owing to existed carbon based radical species and the interaction between oxygen functional groups.[31-34] Nevertheless, EPR signals were notably absent in the Co@CNFs (Figure S9b), suggesting that unpaired electrons are intricately involved in the stabilization process of ultrafine metal nanoparticles.[23, 24] The existence of Co metal nanoparticles was evidenced with the weak diffraction peaks in XRD data (Figure S9a, corresponding to (111) metal Co, JCPDS 15-0806)[35], matching well with the TEM results, Figure 1b). X-ray photoelectron spectroscopy (XPS) data unveil that the nanofibers in Co@CNFs predominantly consist of Co^0 species (778 eV

in the Co 2p spectra, Figure S10 a-b).[36, 37] Nonetheless, oxidized Co ions persists in the particle surface, mainly in the +2 oxidation state (Figure S10 b).[35, 38] This occurrence is primarily attributed to the high reactivity of metal Co, rendering it prone to oxidation in ambient air. A plausible strategy to impede oxidation involves coating a layer of carbon to effectively isolate Co from air. In the presence of ambient air, complete oxidation of Co@CNFs would result in the formation of Co_3O_4, encompassing both metallic Co and Co^{2+}, with carbon releasing as CO_2. Thus, thermogravimetric (TG, Figure S9c) curve indicates a Co content of approximately 26.1 wt%, which matches well with the vibrating sample magnetometer (VSM, Figure S9d). The CNFs didn't show any magnetic intensity (Figure S4c), thus, saturated magnetization testing revealed a magnetic intensity of 35.1 emu g^{-1} for Co@CNFs (Figure S9d), with a metal Co content of approximately 25.8 wt% (35.1/136). Both results underscore the fact that Co@CNFs material encompasses only 0.3 wt% of oxidized cobalt (details in Figure S9). These findings highlight the remarkable effectiveness of nanofibers in preventing the oxidation of metal Co.

Obviously, due to the presence of space charge, the galvanostatic charge-discharge (GCD) curve of Co@CNFs shows a remarkable initial specific charge capacity of up to 610 mAh g^{-1} for lithium storage, with a first-cycle coulombic efficiency reaching 74.2% (Figure 1c), significantly surpassing the theoretical capacity of graphite anode and the CNFs sample (first-cycle charge specific capacity of 330 mAh g^{-1} and coulombic efficiency of 53.9%, Figure S12). Both samples contain the reduction peak at ≤ 1 V (*vs*. Li^+/Li) in the first cycle of the cycling voltammetry data (CV, Figure 1d for Co@CNFs and Figure S12a for CNFs), arising from the reduction of the electrolyte solvent and the formation of the SEI layer. The enhanced lithium storage capacity of Co@CNFs than that of pure CNFs suggests additional lithium storage capacity attributed to the induced nano-sized Co metal particles. However, Co@CNFs also exhibit continuous reduction peaks occurring at higher potential ranges, due to the reduction of Co oxides.[39]

Throughout the entire discharge-charge process, we systematically investigated the lithium storage mechanism of the Co@CNFs anode through an in situ magnetism study (Figure 1e), and the optimal Co@CNFs with the mass loading of 5.4 mg cm^{-2} was selected as the object of study. Non-magnetic carbon anode materials do not exhibit any magnetic changes during cycling.[8, 9] However, in the case of Co@CNFs, the magnetic signal exhibits remarkable variations (Figure 1e), and the voltage and

magnetic curves for the subsequent cycles overlap, in line with previous reports on metal oxide/C composites.[8, 9] The highly reversible magnetic response during the discharge-charge process can be categorized into distinct reversible stages: Initially, in the voltage range of 3 to 2 V (*vs*. Li^+/Li, stage I), the magnetization intensity remains stable, with a minor capacity contribution mainly attributed to lithium ions' surface adsorption. Subsequently, in the discharge voltage range of 1.9 to 0.9 V (*vs*. Li^+/Li, stage II), the increase in magnetization intensity is associated with the reduction of Co^{2+} to ferromagnetic metallic Co^0.[13] However, an interesting phenomenon emerges when the Co@CNFs anode continues discharging to 0.6 V (*vs*. Li^+/Li, stage III). The saturated magnetization intensity remains nearly unchanged or shows a slight reduction. This observation indicates that within the Thomas-Fermi screening length, more electrons accumulate near the Fermi energy level of Co^0 nanoparticles' spin d-band (Figure 1f-g).[12] Consequently, a space charge region forms, capable of accepting electrons, and to maintain charge balance, lithium ions are stored on the particle's surface and near the grain boundaries. During further discharge until 0.01 V (*vs*. Li^+/Li, stage IV), the magnetization of the Co@CNFs electrode increases again. This process involves the transfer of additional electrons from the filled d-band of Co to the surrounding SEI, forming radical anions. Simultaneously, cobalt metal nanoparticles continuously catalyse the formation of a reversible polymer layer.[40] The magnetization shows a slight decrease at the beginning of its charging process (stage V). While the increase in magnetization intensity during the initial stage of charging (stage VI) is attributed to the transfer of electrons from the radical anion at SEI layer to metallic Co^0. Finally, as the voltage increases, the decrease in magnetization intensity (stage VII) indicates the release of spin-polarized electrons from metallic Co^0.

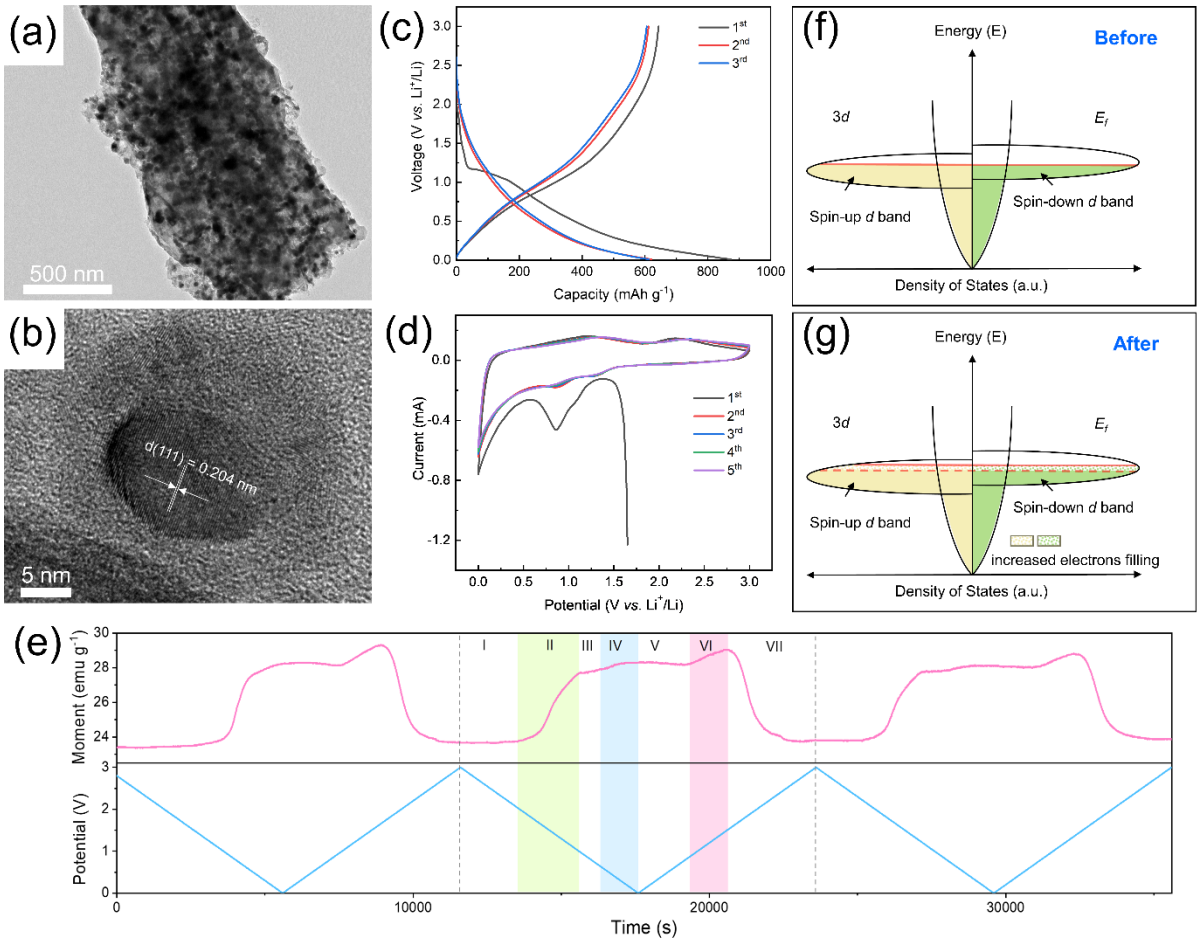

Figure 1. Co@CNFs anode with spin capacitance for lithium storage. (a) TEM; (b) HRTEM; (c) GCD plots measured at 30 mA g^{-1} between 0.01 to 3.0 V (vs. Li^+/Li); (d) CV plots measured at 0.1 mV s^{-1} between 0.01 to 3.0 V (vs. Li^+/Li) of the Co@CNFs electrode, (e) in situ magnetic responses at an applied magnetic field of 3 T to the cycling at a current density of 0.1 A g^{-1} between 0.01~3.0 V (*vs.* Li^+/Li); schematic of the spin-polarized density of states at the surface of ferromagnetic metallic Co grains (f) before and (g) after electron filling into the spin-down d band.

In situ XRD was employed to further investigate the lattice changes occurring in the Co/CNFS anode during charge and discharge processes (Figure 2a). Due to the utilization of a Be film as an X-ray transparent window in the in situ setup, background signals of Be and its oxides were evident in the XRD pattern. The carbon signal observed at approximately 23° 2θ exhibited no displacement, signifying the absence of lithium ion insertion processes. The signal of Co remained unaltered, and no signals of cobalt oxides emerged, indicating that the energy storage process of the Co@CNFs anode is predominantly governed by the spin charge process as discussed earlier. It

is noteworthy that the unchanged results from the in situ XRD tests also suggest the absence of lattice distortion or stress within the electrode material throughout the entire energy storage process, thereby ensuring the integrity of the micro/nanostructure of the electrode during charge and discharge processes. The spin-capacitance effect was further confirmed through ex situ EPR spectra (Figure 2b), where the only carbon-centred radical was observed when the cell was discharged below 0.9 V (*vs*. Li^+/Li). This observation indicates the presence of a radical species (g value of 2.004) within the SEI layer, resulting from electron transfer from metallic Co^0. Thus the lithium storage mechanism of the Co@CNFs includes (Figure 2c): (1) surface cobalt oxide converted into metal Co; (2) electron accumulated at the grain boundaries and surfaces of the metal Co and (3) the reversible interfacial polymeric film grows with the catalysis of Co nanoparticles.

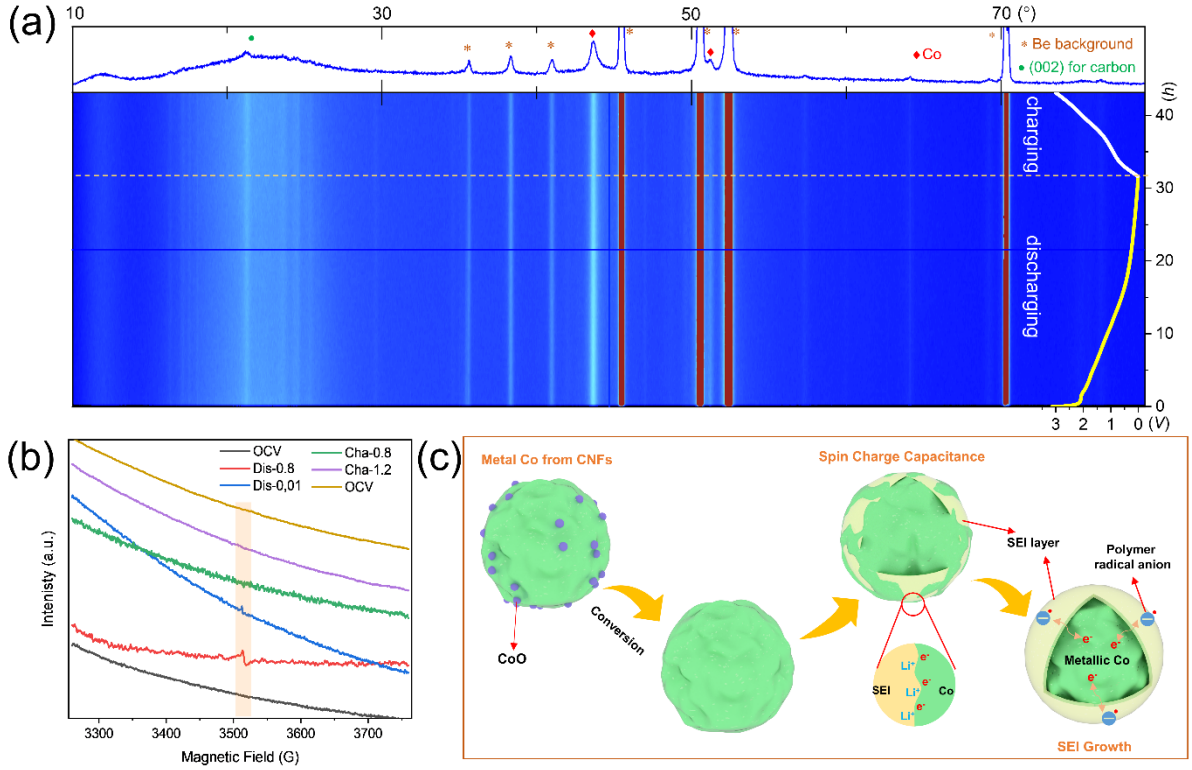

Figure 2. Mechanism study of the Co@CNFs electrode. (a) In situ XRD of the Co@CNFs anode measured at 50 mA g^{-1} from 3 to 0.01 V (*vs*. Li^+/Li); (b) the ex situ EPR spectra of Co@CNFs anode under different potential range; (c) schematic illustrations of space charge process in metallic Co.

The fast lithium storage kinetics of Co@CNFs electrode, owing to the unique spin capacitive mechanism, is revealed by the constant shape of CVs at different scan rates

from 0.1 to 2 mV s^{-1} between 0.01 and 3 V (*vs.* Li^+/Li, Figure S15a). The b values of Co@CNFs, calculated from the peak values of CV curves at different scan rates (Figure 3a), were 0.85 and 0.59 for high and low potential range, respectively (Figure 3b). These values indicate that the dominant lithium storage mechanism in the Co@CNFs anode lies in the surface controlled process within this voltage range.[41] Additionally, we observed an increase in the contribution of capacitive behavior at the higher scan rates according to Conway et al.'s $v/v^{1/2}$ Scan Rate Diagnosis tool[42], ranging from 63.5% at 0.6 mV s^{-1} to 83.8% at 2.0 mV s^{-1} (Figure 3c-d). Thus, there's no surprise that the Co@CNFs (5.4 mg cm^{-2}) shows good rate performance as conclude in Figure 3e. At current densities of 0.1, 0.2, 0.4, 0.6, 0.8, 1.0, 1.5, and 2.0 A g^{-1}, Co@CNFs anodes deliver specific capacities of 610, 573, 511, 486, 465, 451, 423, and 403 mAh g^{-1}, respectively (Figure 3e). When the current density is restored to 0.1 A g^{-1}, its specific capacity remains at 610 mAh g^{-1}, demonstrating good cycling reversibility and stability. Furthermore, Co@CNFs exhibit excellent cycling stability, retaining a specific capacity of 550 mA g^{-1} after 100 cycles (Figure S13b), while under the same testing conditions, CNFs' reversible specific capacity is only 200 mAh g^{-1} after 100 cycles with severe rapid decay (Figure S12d).

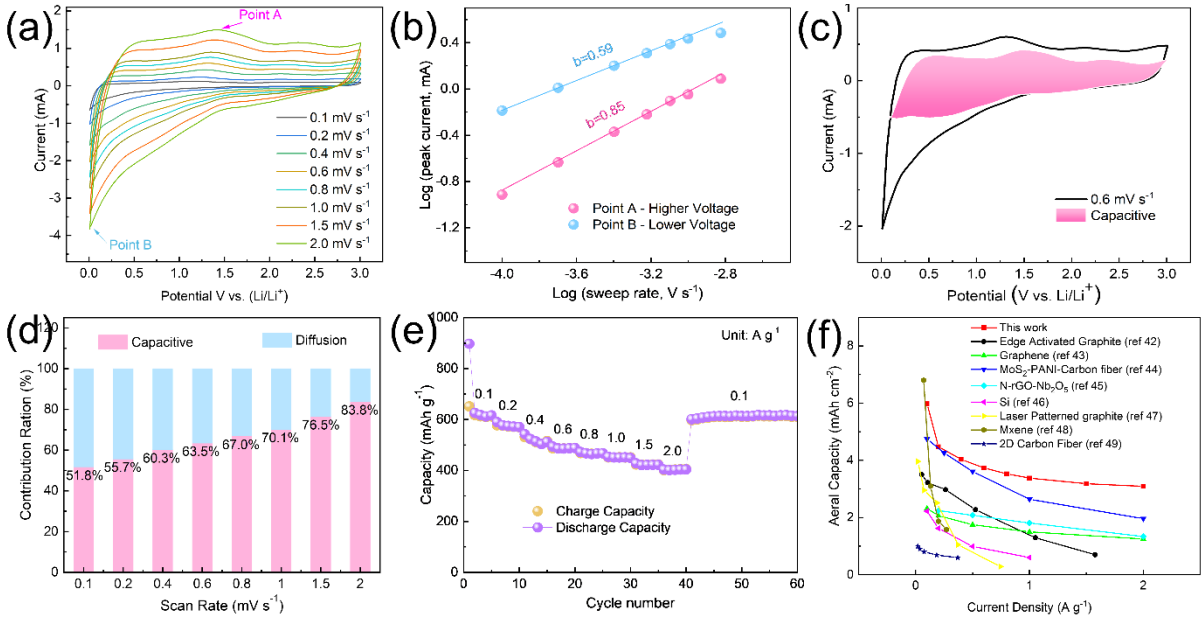

Figure 3. Electrochemical characterization of Co@CNFs. (A) CV curves under various scan rate; (b) log(i) *vs.* log(v) Co@CNFs anode and its corresponding b value obtained from the CV curves under different scan rate; (c) CVs and the capacitive contribution (pink) at a scan rate of 0.6 mV s^{-1}; (d) contribution ratio of capacitive (pink) and

diffusion (blue) controlled to total capacity Co@CNFs anode at various scan rates; (d) rate properties ranging from 0.1 to 2 A g^{-1}; (f) a comparison of the areal performance metrics of Co@CNFs with a mass loading of 6.8 mg cm^{-2} with representative anodes reported.

The electrospinning technique offers a significant advantage of precise control over the thickness. In our investigation, we manipulated the electrospinning time to adjust the Co@CNFs anode loading, ranging from 1 to 6.8 mg cm^{-2} (Figure S13). The corresponding GCD curves are summarized in Figure S14, demonstrating consistent charge storage behaviour across all samples. As the electrode loading increased, the areal charge capacity exhibited continuous growth, with values of 0.67, 1.26, 1.44, 2.27, 3.28, and 5.98 mAh cm^{-2} for mass loadings of 1.0, 2.5, 3.1, 4.0, 5.4, and 6.8 mg cm^{-2} at its first cycle, respectively (Figure SI-14). In comparison with the literature, our high-loading electrode (6.8 mg cm^{-2}) maintains excellent areal capacity even at high rates (3.09 mAh cm^{-2}, Figure 3f).[43-50] The exceptional electrochemical performance of Co@CNFs can be attributed to its unique structural features. The homogeneous distribution of the composite material effectively minimized the dissolution and agglomeration of Co nanoparticles during charge-discharge processes. Furthermore, the abundance of electron and lithium ion transport pathways within the carbon nanofiber facilitated rapid electrochemical reactions. The three-dimensional multi-layered porous structure also contributed positively to electrolyte diffusion, thereby enhancing the overall performance of the Co@CNFs anode. Remarkably, all Co@CNFs electrodes, irrespective of their mass loadings, displayed excellent cycling stability (Figure 4a).

To investigate the factors contributing to the excellent cycling stability of high-loading Co@CNFs electrodes, in situ cross-sectional optical microscopy images under different voltages were examined to analyse the morphological and structural changes of Co@CNFs electrodes during cycling (Figure 4b, c). Experimental observations of a Co@CNFs electrode with a thickness of approximately 500 μm (Figure 4b) indicate that its structure remains unchanged under different charge and discharge voltages (Figure 4c). This matches well with the in situ XRD (Figure 2a) characterization that the charging/discharging process of the Co@CNFs was zero stress without structure crack. Thus, when comparing with the CNFs anodes (Figure S16), which exhibited severe nanofiber fragmentation after cycling, Co@CNFs anodes maintained a well-

preserved nanofiber morphology with a stable three-dimensional interconnected structure (Figure 4d). Moreover, the incorporation of metal Co particles enhances the three-dimensional network structure of the carbon fibres, fortifying the mechanical interconnection between the fibres and endowing Co@CNFs with superior flexibility (Figure S17). Thus the excellent cycling performance of Co@CNFs anodes can be explained by the uniform dispersion of metal Co particles on both the surface and interior of the nanofibers effectively mitigates the volume variation resulting from the oxidation of a minute fraction of metal during charge and discharge cycles.[51, 52] These findings hold considerable implications for advancing the understanding of high-loading Co@CNFs electrodes and their potential application in advanced energy storage systems.

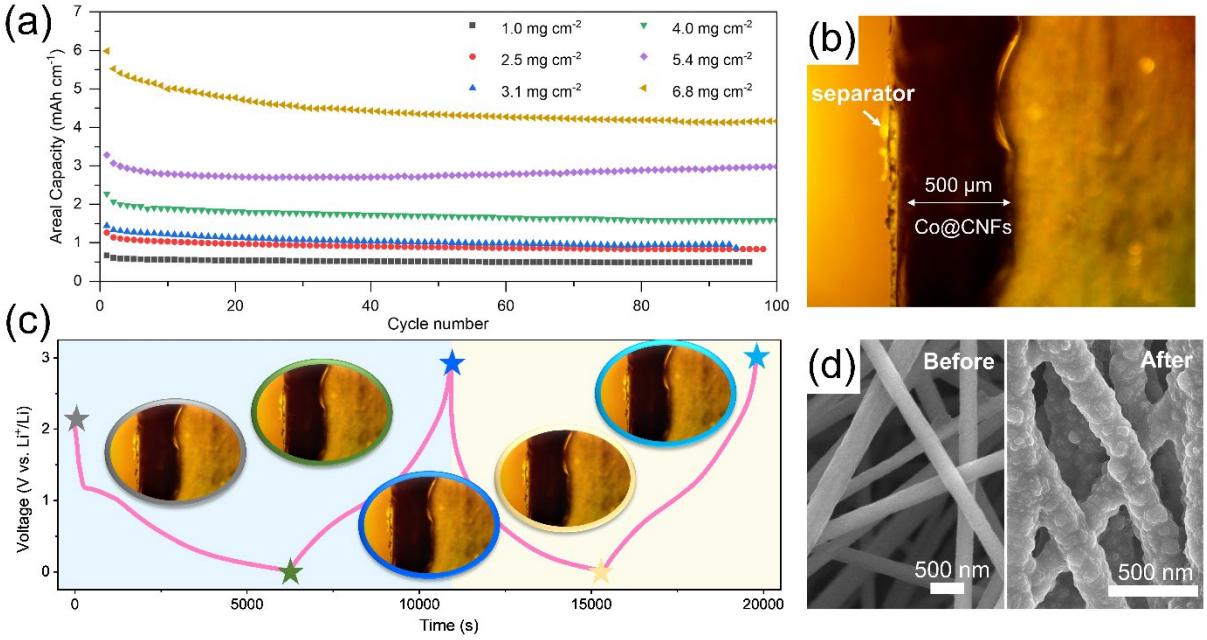

Figure 4. The reasons behind high mass loading anode with stability lithium storage properties. Cycling performance of the Co@CNFs with various mass loading at a current density of 5.4 μA cm^{-2}; (b) cross-section optical microscopy image of the Co@CNFs cell; (c) in situ optical microscopy characterization of the Co@CNFs anode; (d) post-mortem SEM images of Co@CNFs before and after 200 cycles.

Conclusions

A straightforward electrospinning technique was employed to fabricate high-loading and free standing anodes for Li ion batteries. The Co@CNFs anode shows a optimal mass capacity of 610 mA h g^{-1} at 0.1 A g^{-1} (with a loading density of 5.4 mg cm^{-2}) with exceptional rate performance (66% retention at 2C). Moreover, the

Co@CNFs anode shows an areal capacity over 3 mAh cm^{-2} at 2 A g^{-1} when the mass loading is 6.8 mg cm^{-2}. Magnetism and EPR studies have confirmed additional spatial charge storage region within the SEI film due to the Co^0 nanoparticles. The interconnected network structure between nanofibers offered rapid electron and ion transport pathways, while the distinctive spin-charge lithium storage mechanism of metal Co contributed to maintaining the electrode's structural integrity and enhancing its cycling stability. Overall, we have provided a robust strategy to fabricate high-loading and high-capacity anode materials for Li-ion batteries.

Declaration of competing interest

None.

Acknowledgement

This work was financially supported by the National Natural Science Foundation of China (22179145, 21975287, 22005341, and 22138013), Shandong Provincial Natural Science Foundation (ZR2020ZD08 and ZR2020QB128), and the startup support grant from China University of Petroleum (East China).

References

1. Jin, L.; Shen, C.; Shellikeri, A.; Wu, Q.; Zheng, J.; Andrei, P.; Zhang, J.-G.; Zheng, J. P. *Energy & Environmental Science* **2020,** 13, (8), 2341-2362.
2. Wang, R.; Lang, J.; Zhang, P.; Lin, Z.; Yan, X. *Adv. Funct. Mater.* **2015,** 25, (15), 2270-2278.
3. Zhang, H.; Yang, Y.; Ren, D.; Wang, L.; He, X. *Energy Storage Materials* **2021,** 36, 147-170.
4. Asenbauer, J.; Eisenmann, T.; Kuenzel, M.; Kazzazi, A.; Chen, Z.; Bresser, D. *Sustainable Energy & Fuels* **2020,** 4, (11), 5387-5416.
5. Lai, C.-M.; Kao, T.-L.; Tuan, H.-Y. *Journal of Power Sources* **2018,** 379, 261-269.
6. Liang, S.; Cheng, Y.-J.; Zhu, J.; Xia, Y.; Müller-Buschbaum, P. *Small Methods* **2020,** 4, (8), 2000218.
7. Song, Y.; Wang, L.; Sheng, L.; Ren, D.; Liang, H.; Li, Y.; Wang, A.; Zhang, H.; Xu, H.; He, X. *Energy & Environmental Science* **2023,** 16, (5), 1943-1963.
8. Li, Q.; Li, H.; Xia, Q.; Hu, Z.; Zhu, Y.; Yan, S.; Ge, C.; Zhang, Q.; Wang, X.; Shang, X.; Fan, S.; Long, Y.; Gu, L.; Miao, G.-X.; Yu, G.; Moodera, J. S. *Nature Materials* **2021,** 20, (1), 76-83.
9. Li, X.; Su, J.; Li, Z.; Zhao, Z.; Zhang, F.; Zhang, L.; Ye, W.; Li, Q.; Wang, K.; Wang, X.; Li, H.; Hu, H.; Yan, S.; Miao, G.-X.; Li, Q. *Science Bulletin* **2022,** 67, (11), 1145-1153.
10. Li, Z.; Liu, H.; Zhao, Z.; Zhang, Q.; Fu, X.; Li, X.; Gu, F.; Zhong, H.; Pan, Y.; Chen, G.; Li, Q.; Li, H.; Chen, Y.; Gu, L.; Jin, K.; Yan, S.; Miao, G.-x.; Ge, C.; Li, Q. *Adv. Mater.* **2023,** 35, (8), 2207353.
11. Zhao, Z.; Li, Q. *Renewables* **2023,** 1, (2), 169-189.
12. Chen, C.-C.; Maier, J. *Nature Energy* **2018,** 3, (2), 102-108.
13. Li, H.; Hu, Z.; Xia, Q.; Zhang, H.; Li, Z.; Wang, H.; Li, X.; Zuo, F.; Zhang, F.; Wang, X.; Ye, W.; Li, Q.; Long, Y.; Li, Q.; Yan, S.; Liu, X.; Zhang, X.; Yu, G.; Miao, G.-X. *Adv. Mater.* **2021,** 33, (12), 2006629.
14. Kim, H.; Choi, W.; Yoon, J.; Um, J. H.; Lee, W.; Kim, J.; Cabana, J.; Yoon, W.-S. *Chem. Rev.* **2020,** 120, (14), 6934-6976.
15. Lu, Y.; Chen, J. *Nature Reviews Chemistry* **2020,** 4, (3), 127-142.
16. Chen, Y.; Key, J.; O'Regan, K.; Song, T.; Han, Y.; Kendrick, E. *Chem. Eng. J.* **2022,** 450, 138275.
17. Chen, R.; Yu, M.; Sahu, R. P.; Puri, I. K.; Zhitomirsky, I. *Advanced Energy Materials* **2020,** 10, (20), 1903848.

18. Wu, F.; Liu, M.; Li, Y.; Feng, X.; Zhang, K.; Bai, Y.; Wang, X.; Wu, C. *Electrochemical Energy Reviews* **2021,** 4, (2), 382-446.
19. Kim, Y.; Kim, M.; Lee, T.; Kim, E.; An, M.; Park, J.; Cho, J.; Son, Y. *Electrochem. Commun.* **2023,** 147, 107437.
20. Dou, Y.; Zhang, W.; Kaiser, A. *Advanced Science* **2020,** 7, (3), 1902590.
21. Chang, X.; Zhou, X.; Ou, X.; Lee, C.-S.; Zhou, J.; Tang, Y. *Advanced Energy Materials* **2019,** 9, (47), 1902672.
22. Teng, X.; Li, X.; Yang, H.; Guan, L.; Li, Y.; Yun, H.; Li, Z.; Li, Q.; Hu, H.; Wang, Z.; Wu, M. *Chemical Science* **2023,** 14, (9), 2455-2460.
23. Chen, Y.; Egan, G. C.; Wan, J.; Zhu, S.; Jacob, R. J.; Zhou, W.; Dai, J.; Wang, Y.; Danner, V. A.; Yao, Y.; Fu, K.; Wang, Y.; Bao, W.; Li, T.; Zachariah, M. R.; Hu, L. *Nature Communications* **2016,** 7, (1), 12332.
24. Yang, C.; Ko, B. H.; Hwang, S.; Liu, Z.; Yao, Y.; Luc, W.; Cui, M.; Malkani, A. S.; Li, T.; Wang, X.; Dai, J.; Xu, B.; Wang, G.; Su, D.; Jiao, F.; Hu, L. *Science Advances* 6, (17), eaaz6844.
25. Qiu, S.; Xiao, L.; Sushko, M. L.; Han, K. S.; Shao, Y.; Yan, M.; Liang, X.; Mai, L.; Feng, J.; Cao, Y.; Ai, X.; Yang, H.; Liu, J. *Advanced Energy Materials* **2017,** 7, (17), 1700403.
26. Wang, B.; Likodimos, V.; Fielding, A. J.; Dryfe, R. A. W. *Carbon* **2020,** 160, 236-246.
27. Stankovich, S.; Dikin, D. A.; Piner, R. D.; Kohlhaas, K. A.; Kleinhammes, A.; Jia, Y.; Wu, Y.; Nguyen, S. T.; Ruoff, R. S. *Carbon* **2007,** 45, (7), 1558-1565.
28. Ferrari, A. C.; Robertson, J. *PhRvB* **2000,** 61, (20), 14095-14107.
29. Surekha, G.; Krishnaiah, K. V.; Ravi, N.; Padma Suvarna, R. *Journal of Physics: Conference Series* **2020,** 1495, (1), 012012.
30. Sadezky, A.; Muckenhuber, H.; Grothe, H.; Niessner, R.; Pöschl, U. *Carbon* **2005,** 43, (8), 1731-1742.
31. Menachem, C.; Wang, Y.; Flowers, J.; Peled, E.; Greenbaum, S. G. *Journal of Power Sources* **1998,** 76, (2), 180-185.
32. Wang, B.; Fielding, A. J.; Dryfe, R. A. W. *The Journal of Physical Chemistry C* **2019,** 123, (36), 22556-22563.
33. Ćirić, L.; Sienkiewicz, A.; Djokić, D. M.; Smajda, R.; Magrez, A.; Kaspar, T.; Nesper, R.; Forró, L. *physica status solidi (b)* **2010,** 247, (11-12), 2958-2961.
34. Diamantopoulou, A.; Glenis, S.; Zolnierkiwicz, G.; Guskos, N.; Likodimos, V. *Journal of Applied Physics* **2017,** 121, (4), 043906.
35. Yang, Q.; Feng, C.; Liu, J.; Guo, Z. *Applied Surface Science* **2018,** 443, 401-406.
36. Bazylewski, P.; Boukhvalov, D. W.; Kukharenko, A. I.; Kurmaev, E. Z.; Hunt, A.; Moewes, A.; Lee, Y. H.; Cholakh, S. O.; Chang, G. S. *RSC Advances* **2015,** 5, (92), 75600-75606.
37. Zheng, L.; Sun, X.; Chen, L.; Bao, C.; Luo, W.; Huang, N.; Sun, P.; Sun, Y.; Fang, L.; Wang, L. *JMatS* **2016,** 51, (8), 4150-4159.
38. Zhang, C.-L.; Lu, B.-R.; Cao, F.-H.; Yu, Z.-L.; Cong, H.-P.; Yu, S.-H. *Journal of Materials Chemistry A* **2018,** 6, (27), 12962-12968.
39. Meng, Y.; Wang, G.; Xiao, M.; Duan, C.; Wang, C.; Zhu, F.; Zhang, Y. *JMatS* **2017,** 52, (22), 13192-13202.
40. Laruelle, S.; Grugeon, S.; Poizot, P.; Dollé, M.; Dupont, L.; Tarascon, J. M. *Journal of The Electrochemical Society* **2002,** 149, (5), A627.
41. He, T.; Kang, X.; Wang, F.; Zhang, J.; Zhang, T.; Ran, F. *Materials Science and Engineering: R: Reports* **2023,** 154, 100737.
42. Liu, T. C.; Pell, W. G.; Conway, B. E.; Roberson, S. L. *Journal of The Electrochemical Society* **1998,** 145, (6), 1882.
43. Kim, N.; Chae, S.; Ma, J.; Ko, M.; Cho, J. *Nature Communications* **2017,** 8, (1), 812.
44. Xu, Y.; Lin, Z.; Zhong, X.; Papandrea, B.; Huang, Y.; Duan, X. *Angew. Chem. Int. Ed.* **2015,** 54, (18), 5345-5350.
45. Lingappan, N.; Jeon, I.; Lee, W. *Journal of Alloys and Compounds* **2024,** 979, 173611.
46. Li, X.; Hou, Y.; Yin, Z.-H.; Xiang, S.-B.; Yin, C.; Yin, Z. *Journal of Energy Storage* **2023,** 73, 109003.
47. Wang, Y.; Xu, H.; Chen, X.; Jin, H.; Wang, J. *Energy Storage Materials* **2021,** 38, 121-129.
48. Dubey, R.; Zwahlen, M.-D.; Shynkarenko, Y.; Yakunin, S.; Fuerst, A.; Kovalenko, M. V.; Kravchyk, K. V. *Batteries & Supercaps* **2021,** 4, (3), 464-468.
49. Kim, S. J.; Naguib, M.; Zhao, M.; Zhang, C.; Jung, H.-T.; Barsoum, M. W.; Gogotsi, Y. *Electrochim. Acta* **2015,** 163, 246-251.
50. Jagdale, P.; Nair, J. R.; Khan, A.; Armandi, M.; Meligrana, G.; Hernandez, F. R.; Rusakova, I.; Piatti, E.; Rovere, M.; Tagliaferro, A.; Winter, M.; Gerbaldi, C. *Electrochim. Acta* **2021,** 368, 137644.
51. Yao, X.; Li, J.; Zhu, Y.; Li, L.; Zhang, W. *Composites Part B: Engineering* **2020,** 193, 108058.
52. Wu, M.; Tian, X.; Yang, W.; Guo, B.; Guo, J. *Electrochim. Acta* **2022,** 411, 140090.